The Astrophysical Journal, 859:70 (9pp), 2018 May 20 https://doi.org/10.3847/1538-4357/aabd79

The Origin of the Optical Flashes: The Case Study of GRB 080319B and GRB 130427A

N. Fraija[1] and P. Veres[2]
[1] Instituto de Astronomía, Universidad Nacional Autónoma de México, Circuito Exterior, C.U., A. Postal 70-264, 04510 Cd. de México, México; nifraija@astro.unam.mx, pv0004@uah.edu
[2] Center for Space Plasma and Aeronomic Research (CSPAR), University of Alabama in Huntsville, Huntsville, AL 35899, USA
Received 2017 December 25; revised 2018 March 20; accepted 2018 April 5; published 2018 May 24

Abstract

Correlations between optical flashes and gamma-ray emissions in gamma-ray bursts (GRBs) have been searched in order to clarify the question of whether these emissions occur at internal and/or external shocks. Among the most powerful GRBs ever recorded are GRB 080319B and GRB 130427A, which at early phases presented bright optical flashes possibly correlated with γ-ray components. Additionally, both bursts were fortuitously located within the field of view of the TeV γ-ray Milagro and HAWC observatories, and although no statistically significant excess of counts were collected, upper limits were placed on the GeV–TeV emission. Considering the synchrotron self-Compton emission from internal shocks and requiring the GeV–TeV upper limits, we found that the optical flashes and the γ-ray components are produced by different electron populations. Analyzing the optical flashes together with the multiwavelength afterglow observation, we found that these flashes can be interpreted in the framework of the synchrotron reverse shock model when outflows have arbitrary magnetizations.

Key words: gamma-ray burst: individual (GRB 080319B, GRB 130427A) – radiation mechanisms: nonthermal

1. Introduction

Gamma-ray bursts (GRBs) are classified as some of the most energetic events in the universe. Our understanding of GRBs has improved significantly in the last 15 years. Observations have firmly established that GRB prompt phases and their afterglows arise from highly relativistic and collimated outflows (Panaitescu & Kumar 2002; Taylor et al. 2004). Based on photometric and spectroscopic observations, long GRBs (lGRBs) have usually been associated with the core collapse of massive stars (Hjorth et al. 2003; Woosley & Bloom 2006; Hjorth & Bloom 2012) and short GRBs to the merger of compact objects (Eichler et al. 1989; Narayan et al. 1992; Lee et al. 2004, 2005).

Among the fundamental questions that are not answered yet is the physical origin of the prompt emission in GRBs. Although it is still uncertain, a typical GRB prompt spectrum is nonthermal and generally well modeled by a so-called Band function (Band et al. 1993), which depends on three parameters: a low-energy power-law index α, a high-energy power-law index β, and a spectral break energy $E_p^{\rm obs}$, which defines the smooth transition between the two power laws. The observations of GRB prompt emission with low-energy spectral slopes that are inconsistent with synchrotron (Cohen et al. 1997; Preece et al. 1998; Ghisellini et al. 2000; Preece et al. 2002) supply further information to consider inverse Compton scattering. Zhang et al. (2016) suggested that for the origin of the observed GRB prompt emission, at least some, if not all, Band-like GRB spectra with typical parameter values can be interpreted as synchrotron radiation from accelerated electrons in shock waves. Such internal shocks (IS) occurred if the ejection process by the central source is highly variable (Rees & Meszaros 1994; Panaitescu & Mészáros 2000; Guetta & Granot 2003; Pe'er & Waxman 2004; Asano & Inoue 2007; Gupta & Zhang 2007; Ando et al. 2008). The observation of high-energy spectral components in the GRB prompt phase can provide strong constraints on present models. Some authors have claimed that the high-energy emission with photons $>$100 MeV during the prompt phase (before T_{90}) has an internal origin similar to its lower counterpart energies (He et al. 2011; Liu & Wang 2011; Maxham et al. 2011; Zhang et al. 2011).

Optical flashes have been widely discussed in the literature (see Kumar & Zhang 2015). Using standard assumptions such as the forward- and reverse-shocked shells carry comparable energy, optical flashes are described by synchrotron emission from reverse shock (RS), which is shown as a single peak (Chevalier & Li 2000; Kobayashi 2000; Kobayashi & Zhang 2003; Zhang et al. 2003; Zhang & Kobayashi 2005), although if the central engine emits slowly moving material the RS could survive up to weeks (Genet et al. 2007; Uhm & Beloborodov 2007). Mészáros & Rees (1997) proposed that optical flashes might result from IS even if these flashes from IS are nearly two orders of magnitude weaker than those due to the RS. The authors showed that, with beaming factors of $\sim 10^{-2}$, it is possible to have flashes as bright as ninth magnitude for $z \sim 1$ (Mészáros & Rees 1999; Kumar & Piran 2000). Considering the FS propagating into the pre-accelerated and pair-loaded environment, some authors have proposed that FS at its early stage could explain the early optical emission (Mészáros et al. 2001; Beloborodov 2002). Early observations of GRB afterglows would offer to clarify the question whether the early emission takes place at IS or ES.

Prompt observations in the optical frequencies remain difficult due to a lack of good temporal coverage. However, strong evidence in favor of a bright additional component at low energies is given by GRB 080319B and GRB 130427A. These bursts are among the brightest and most energetic GRBs, which were observed by several satellites and ground-based instruments. Racusin et al. (2008b) found that for GRB 080319B both optical and gamma-ray bands were mildly correlated, leading to both emissions originating in the same physical region, and Vestrand et al. (2014) reported that the optical and very-high-energy (VHE) gamma-ray emissions showed a close correlation during the first 7000 s.

In this paper, we analyze the origin of optical flashes present in the light curve (LC) of GRB 080319B and GRB 130427A.

We consider the GeV–MeVγ-ray, X-ray, and optical data together with the GeV–TeV upper limits derived by Milagro and HAWC experiments to constrain the synchrotron self-Compton (SSC) models from IS and early-afterglow ES. The paper is arranged as follows: in Section 2, we give a brief description of GRB 080319B and GRB 130427A observations; in Section 3, we present a model based on IS and early-afterglow ES to fit data; in Section 4, we discuss our results, and brief conclusions are given in Section 5.

2. Properties of GRB 080319B and GRB 130427A

In the following subsections, we present a brief description of the observations performed around GRB 080319B and GRB 130427A.

2.1. GRB 080319B

On 2008 March 19, one of the brightest and most energetic bursts, GRB 080319B, was observed by several satellites and ground-based instruments. The *Swift*-Burst Alert Telescope (BAT; 15–350 keV) triggered on GRB 080319B at $T_0 =$ 06:12:49 UT (Racusin et al. 2008a). The burst direction was within the field of view of the BAT for 1080 s, placing strong limits on any precursor emission. This burst was simultaneously detected with the Konus gamma-ray detector (20 keV–15 MeV) on board the *Wind* satellite (Golenetskii et al. 2008). Both *Swift*-BAT and Konus-Wind (KW) LCs showed a complex and a strongly energy-dependent structure, lasting approximately 57 s (Racusin et al. 2008b). The time-averaged KW gamma-ray spectrum was well fit using a Band function (Band et al. 1993), with $\alpha = -0.855^{-0.014}_{-0.013}$, $\beta = -3.59^{+0.32}_{-0.62}$, and $E_p^{\rm obs} = 675 \pm 22$ keV ($\chi^2/{\rm dof} = 110.4/80$). This burst had a peak flux of $(2.26 \pm 0.21) \times 10^{-5}$ erg cm^{-2} s^{-1}, a gamma-ray fluence of $(6.13 \pm 0.13) \times 10^{-4}$ erg cm^{-2} and an isotropic equivalent gamma-ray energy release of 1.3×10^{54} erg in the energy range of 20 keV–7 MeV (Racusin et al. 2008b).

The wide-field robotic optical telescope Pi of the Sky (Ćwiok et al. 2007; Cwiok et al. 2008), and the wide-field robotic instrument Telescopio Ottimizzato per la Ricerca dei Transienti Ottici RApidi (TORTORA, which is attached to the 60 cm robotic optical/near-infrared Rapid Eye Mount (REM; Zerbi et al. 2001) telescope located at La Silla, Chile), coincidentally had this burst within their fields of view at the time of the explosion (Pagani et al. 2008). Pi of the Sky observed the bright optical transient from $T_0 + 2.75$ s to it faded below threshold to ~12th magnitude after 5 minutes (Bloom et al. 2009). TORTORA measured the brightest portion of the optical flash with high time resolution enabling to do detailed comparisons between the prompt optical and gamma-ray emission (Racusin et al. 2008b). The *Swift* and REM telescopes both initiated automatic slews to the burst, resulting in optical observations in the *R* and UV bands (1700–6000 Å, with the *Swift* UltraViolet-Optical Telescope, UVOT) beginning at $T_0 + 51$ s and $T_0 + 68$ s, respectively. The *Swift* X-ray Telescope (XRT) began observing the burst at $T_0 + 51$ s, providing time-resolved spectroscopy in the 0.3–10 keV band. Subsequent optical spectroscopy by Gemini-N and the Hobby–Eberly Telescope confirmed the redshift of $z = 0.937$ (Racusin et al. 2008b).

Finally, this burst was fortuitously located within the field of view of the Milagro observatory. Although no evidence for emission was found in the Milagro data, upper limits on the flux above 10 GeV were derived (Abdo et al. 2012).

2.2. GRB 130427A

On 2013 April 27, one of the most energetic bursts, GRB 130427A, was observed from radio wavelengths to GeV gamma-rays. GRB 130427A triggered the Gamma-ray Burst Monitor (GBM) on board the Fermi satellite at $T_0 =$ 07:47:06.42 UTC (von Kienlin 2013). The Large Area Telescope (LAT) followed up this burst until it became eclipsed by the Earth 715 s after the GBM trigger. In addition to a bright peak at $T_0 \sim 15$ s, this burst displayed the highest fluence with isotropic energy of $\sim 1.4 \times 10^{54}$ erg and the highest energy photons ever detected, 73 GeV and 95 GeV observed at 19 s and 244 s, respectively (Ackermann et al. 2014). Rapid Telescope for Optical Response (Wren et al. 2010) reported on a bright optical flash that was temporally correlated with the LAT peak. This optical flash had a magnitude of 7.03 ± 0.03 and was detected in the time interval of [14–16 s] after the GBM trigger (Vestrand et al. 2014).

BAT triggered on the ongoing burst at 07:47:57.51 UTC, and UVOT and XRT started observations at $\sim T_0 + 181$ s and $\sim T_0 + 195$ s, respectively (Maselli et al. 2014). The LC exhibited by the BAT instrument showed a complex structure with a duration of ~20 s. Due to its extremely bright prompt emission, this burst was also detected by other satellites (SPI-ACS/*INTEGRAL* (Pozanenko et al. 2013), AGILE (Verrecchia et al. 2013), KW (Golenetskii et al. 2013), NuSTAR (Kouveliotou et al. 2013), and *RHESSI* (Smith et al. 2013)) and multiple ground- and space-based follow-up facilities (MAXI/GSC (Kawamuro et al. 2013) and VLT/X-shooter (Flores et al. 2013)). Optical spectroscopy from Gemini-north found the redshift of the GRB to be $z = 0.34$ (confirmed later by VLT/X-shooter Flores et al. 2013), revealing the closeness to Earth (Levan et al. 2013) and the optical/near-infrared (NIR) counterpart observed with the *Hubble Space Telescope* suggested the association of GRB 130427A with a Type Ic supernova (SN2013cq; Levan et al. 2013; Xu et al. 2013).

The high-altitude water Cherenkov observatory (HAWC; Lennarz & Taboada 2013; Abeysekara et al. 2015a) followed up this burst and although GeV–TeV photons were not detected, upper limits in the flux were derived.

2.3. Constraints Provided by TeV Observatories

2.3.1. Milagro Observatory

Before, during, and after the prompt phase of GRB 080319B, the Milagro observatory simultaneously collected data from the two data acquisition (DAQ) systems, the main and scaler system (Abdo et al. 2012). The main DAQ system reads out coincident signals and reconstructs the direction and energy of the atmospheric shower events. The scaler DAQ counts the hits in each photomultiplier tube and searches for a statistical excess over the background. Data from both DAQ systems were analyzed to get the upper limits on the GeV–TeV γ-ray flux. For instance, the standard analysis consisted of searching for an excess of events above the background in temporal and spatial coincidence with the main γ-ray pulse reported by Konus on board the Wind satellite (Golenetskii et al. 2008). This analysis showed no significant excess of events (30 events collected with a predicted background of

Table 1
Observed Quantities for GRB 080319B and GRB 130427A

Parameter	GRB 080319B	GRB 130427A
Isotropic energy ($\times 10^{54}$ erg)	1.3	1.2
Redshift	0.937	0.34
Period of peak correlations (s)[a]	2.75–57.0	9.31–19.31
L_x/L_{op}[b]	15.3	89.1
Low-energy power-law index (α)	0.833	0.789
High-energy power-law index (β)	3.499	3.06
Spectral break energy (E_p^{obs})	651	830

Notes.
[a] They are taken from Racusin et al. (2008b) and Vestrand et al. (2014) for GRB 080319B and GRB 130427A, respectively. These correspond to the periods where optical flashes and the γ-ray components show close correlations.
[b] The X-ray luminosities were reported by *Swift*-BAT (Band 15–350 keV; Maselli et al. 2014). The magnitude of the optical flashes was 5.3 in the *V*-band and 7.03 in the *R*-band for GRB 080319B (Racusin et al. 2008b) and GRB 130427A (Vestrand et al. 2014), respectively.

29.7) associated during the main γ-ray pulse reported by Konus.

2.3.2. HAWC Observatory

HAWC with an order of magnitude better sensitivity and angular resolution than its predecessor, the Milagro observatory, could follow-up GRB 130427A (Abeysekara et al. 2015a). This burst took place under disadvantageous conditions for HAWC observation (it was running 10% of the final detector). Based on the trigger time, HAWC selected eight different time periods to search for photons in the energy range of 0.5 GeV–1 TeV. In the selected periods, no statistically significant excesses were found and upper limits were placed. These upper limits were converted to integral flux upper limits using the HAWC effective area for the declination of GRB 130427A.

2.4. Comparison: GRB 080319B and GRB 130427A

Given some similarities, we summarize in Table 1 the relevant observational quantities for GRB 080319B and GRB 130427A.

3. Emission Processes

To study the optical flash, we show a model based on the IS and the early-afterglow ES. The convention $Q_x = Q/10^x$ is used in c.g.s. units with the universal constants $c = \hbar = 1$ in natural units.

3.1. Internal Shocks

In the standard fireball model, inhomogeneities in the jet lead to internal shell collisions occurring at $r_j = 2\Gamma^2 t_v$, with t_v being the variability timescale of the engine and Γ being the bulk Lorentz factor. The total energy density $U = 1/(8\,\pi\, m_p)\Gamma^{-4} L_j\, t_v^{-2}$ in the internal shock is equipartitioned to amplify the magnetic field and to accelerate particles through the microphysical parameters ϵ_B and ϵ_e, respectively. L_j is the isotropic equivalent kinetic luminosity and m_p is the proton mass. Once the magnetic field is amplified, relativistic electrons are efficiently cooled down via synchrotron radiation and IC scattering.

Taking into account the bright optical and the MeV γ-ray components, it is naturally thought that synchrotron and IC radiation could describe the optical flash and the MeV γ-ray component, respectively (Panaitescu & Mészáros 2000; Kumar & McMahon 2008). Considering this assumption and requiring the Band function (Band et al. 1993), then the Compton Y_1 parameter, defined as the radio of IC scattering to synchrotron energy losses, is

$$Y_1 \simeq \frac{E_{\gamma,p}^{ssc1}\, F_\nu^{ssc1}}{E_{\gamma,p}^{syn}\, F_\nu^{syn}}, \tag{1}$$

where $E_{\gamma,p}^{syn}$ is the synchrotron energy defined by

$$E_{\gamma,p}^{syn} = \frac{3\, q_e}{2\pi\, m_e}(1+z)^{-1}\,\Gamma\, B'\,\gamma_e^2, \tag{2}$$

with the comoving magnetic field $B' = \epsilon_B^{1/2}\,\Gamma^{-2}\,L_j^{1/2}\,t_\nu^{-1}$, the peak synchrotron flux

$$F_\nu^{syn} = \frac{m_e \sigma_T}{12\pi q_e}(1+z)\Gamma\, B'\, N_e\, D^{-2}, \tag{3}$$

and $E_{\gamma,p}^{ssc1} \simeq \gamma_e^2\, E_{\gamma,p}^{syn}$. Here, m_e is the electron mass, q_e is the elementary charge, σ_T is the Thomson cross section, D is the luminosity distance, N_e is the number of radiating electrons, and $\gamma_e = \left(\frac{Y_1}{\tau}\right)^{\frac{1}{2}}$ is the electron Lorentz factor (Zou et al. 2009) with τ the optical thickness of the source to Thomson scattering given by

$$\tau = \frac{\sigma_T\, N_e}{4\pi R^2}. \tag{4}$$

From Equations (1) to (4), the emitting radius is

$$R = \sqrt{\frac{9q_e^2}{2\pi m_e^2}}\,(1+z)^{-1}\, D\,\gamma_e^2\,(F_\nu^{ssc1} E_{\gamma,p}^{ssc1})^{1/2}\, Y_1^{-1}\,[E_{\gamma,p}^{syn}]^{-1}. \tag{5}$$

If the MeV γ-ray emission is stronger than the optical flash, then a third spectral emission arising from the second-order IC scattering would be expected (Kumar & Panaitescu 2008). The second inverse Compton scattering takes place just above the Klein–Nishina (KN) limit, where the electron scattering cross section is $\sim 0.4\sigma_T$. The KN suppression becomes important only at $E_{KN} > 132.9\left(\frac{10\,\mathrm{eV}}{E_{\gamma,p}^{syn}}\right)^{-1/2}\,\Gamma_3$ GeV. Hence, the twice-scattered photon takes all the electron energy, then the third spectral component peaks at energies around

$$E_{\gamma,p}^{ssc2} \simeq \frac{[E_{\gamma,p}^{ssc1}]^2}{E_{\gamma,p}^{syn}}, \tag{6}$$

and theoretically, the Compton Y_2 parameter is given by (Kumar & Panaitescu 2008)

$$Y_2 = 0.4 m_e (1+z)^{-1}\,\Gamma\, E_{\gamma,p}^{ssc1}\,\gamma_e^{-1}\, Y_1. \tag{7}$$

Observationally, the Compton parameter of second-order IC scattering can be obtained through

$$Y_2 \simeq \frac{E_{\gamma,p}^{ssc2}\, F_\nu^{ssc2}}{E_{\gamma,p}^{ssc1}\, F_\nu^{ssc1}}, \tag{8}$$

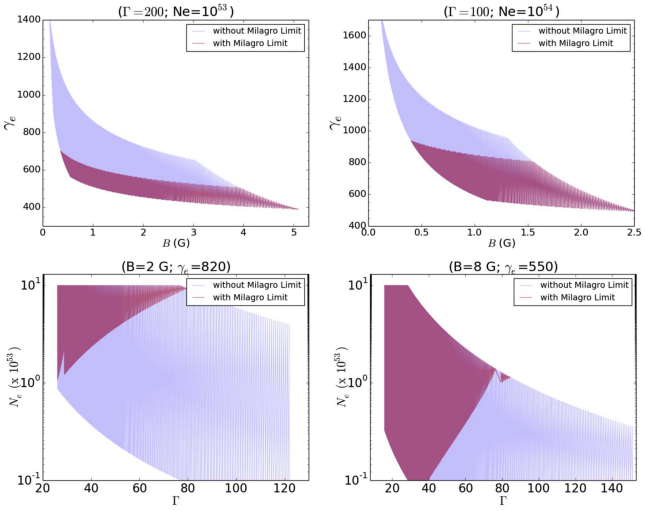

Figure 1. Range of parameters found using the observables of GRB 080319B with and without Milagro limits. Upper panels show the electron Lorentz factor as a function of magnetic field and lower panels show the electron density as a function of bulk Lorentz factor.

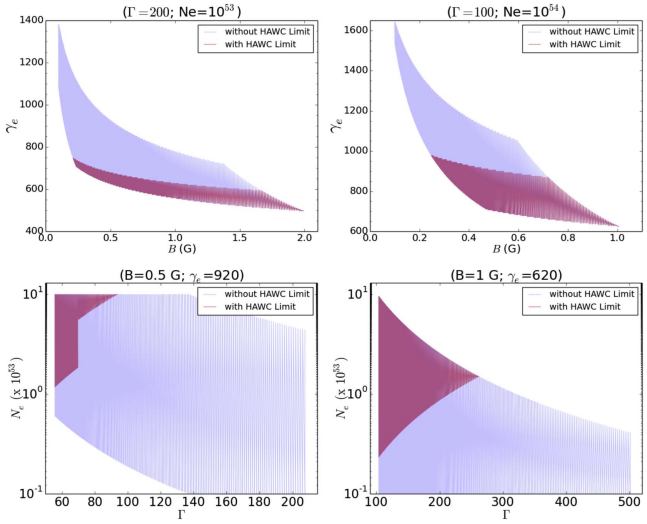

Figure 2. Range of parameters found using the observables of GRB 130427A with and without HAWC limits. Upper panels show the electron Lorentz factor as a function of magnetic field and lower panels show the electron density as a function of bulk Lorentz factor.

where $E^{\rm ssc2}_{\gamma,{\rm p}}$ is the corresponding Band function peak energy in the GeV–TeV energy range given by $E^{\rm ssc2}_{\gamma,{\rm p}} \simeq \gamma_e^2\, E^{\rm ssc1}_{\gamma,{\rm p}}$ and $E^{\rm ssc2}_{\gamma,{\rm p}}\, F^{\rm ssc2}_{\nu}$ are obtained from the GeV–TeV limits derived by Milagro and HAWC observatories.

3.2. Are the HAWC and Milagro Upper Limits Restrictive?

The upper limits set by Milagro and HAWC γ-ray observatories in the range of tens of GeV to 1 TeV are used for GRB 080319B and GRB 130427A, respectively, in order to constrain the range of parameters of electron Lorentz factor (γ_e), bulk Lorentz factor (Γ), number of radiating electrons (N_e) and magnetic field (B'). The restrictions of these parameters are given using the second-order IC scattering that originated in IS, which was described above.

Figures 1 and 2 show the range of parameters found using the observables of GRB 080319B and GRB 130427A with (red color) and without (blue color) Milagro and HAWC upper limits, respectively, with the following assumptions: (i) the optical flash peaks at $0.5 \leqslant E_{\rm opt} \leqslant 1.5$ eV with a corresponding flux in the range of $10^{-8} \leqslant F_{\nu,{\rm opt}} \leqslant 10^{-7}$ erg cm^{-2} s^{-1}, and (ii) the γ-ray emission peaks at $0.1 \leqslant E_\gamma \leqslant 0.6$ MeV with a corresponding flux in the range of $5 \times 10^{-6} \leqslant F_\nu$, $\gamma \leqslant 5 \times 10^{-5}$ erg cm^{-2} s^{-1}.

Upper panels in Figure 1 show the electron Lorentz factor as a function of magnetic field. Left-hand panel exhibits that electron Lorentz factor and magnetic field are in the ranges of $400 \lesssim \gamma_e \lesssim 1400$ and $0.5 \lesssim B' \lesssim 5$ G, respectively, for $\Gamma = 200$ and $N_e = 10^{53}$ and the right-hand panel displays that are in the ranges of $500 \lesssim \gamma_e \lesssim 1600$ and $0.3 \lesssim B' \lesssim 2.5$ G for $\Gamma = 100$ and $N_e = 10^{54}$. Panels show that the electron Lorentz factors larger than $\gamma_e \gtrsim 700$ (left) and $\gamma_e \gtrsim 950$ (right) are restricted when the Milagro upper limits are taken into consideration.

Lower panels in Figure 2 show the number of radiating electrons as a function of bulk Lorentz factor. Left-hand panel exhibits that the number of radiating electrons and the bulk Lorentz factor are in the ranges of $0.1 \lesssim N_e \lesssim 10 \times 10^{53}$ and $60 \lesssim \Gamma \lesssim 210$ for $B' = 0.5$ G and $\gamma_e = 920$, and the right-hand panel displays those in the ranges of $0.1 \lesssim N_e \lesssim 8 \times 10^{53}$ and $105 \lesssim \Gamma \lesssim 500$ for $B' = 1$ G and $\gamma_e = 620$. Panels show that bulk Lorentz factors larger than $\Gamma \gtrsim 100$ (left) and $\Gamma \gtrsim 250$ (right) are forbidden when the HAWC upper limits are considered.

Figures 1 and 2 show that the HAWC and Milagro upper limits are restrictive when the second-order IC scattering is considered.

3.3. Early-afterglow External Shocks

The afterglow emission begins at a distance where most of the energy carried by the outflow is transferred to the circumburst medium (Rees & Meszaros 1992), generating forward and RSs (Rees & Meszaros 1994; Meszaros & Rees 1994). We will use the subscripts f and r to refer, throughout this paper, to the forward and RSs, respectively. In this subsection, we are going to adopt the wind afterglow model $\rho = Ar^{-2}$ with $A = A_\star\, (5.0 \times 10^{11})$ g cm^{-1} proposed to describe the early multiwavelength emission in GRB 130427A (Fraija et al. 2016a).

3.3.1. Light Curves from Forward Shock Emission

Once the outflow has been accelerated relativistically and has gone into the stratified wind, it begins to be decelerated, leading to a continuous softening of the synchrotron forward shock spectrum. The synchrotron spectrum is usually obtained using the deceleration, cooling, and acceleration timescales, and the maximum flux given by the peak spectral power (see, e.g., Chevalier & Li 2000). Given the synchrotron spectral breaks (Fraija et al. 2016a), the LCs in the fast- and slow-cooling regime are obtained through the synchrotron spectrum. The LCs in the fast-cooling regime are

$$[F_{\nu,{\rm f}}]^{\rm syn} = \begin{cases} F_{\nu,{\rm fl}}\, t_1^{-\frac{1}{4}}, & E^{\rm syn}_{\rm c,f} < E_\gamma < E^{\rm syn}_{\rm m,f}, \\ F_{\nu,{\rm fh}}\, t_1^{-\frac{3p-2}{4}}, & E^{\rm syn}_{\rm m,f} < E_\gamma < E^{\rm syn}_{\rm max,f}, \end{cases} \quad (9)$$

where $F_{\nu,\rm fh}$ is

$$F_{\nu,\rm fh} = 2.8 \times 10^{-1}\,{\rm mJy}\,k_f^{-1}(1+z)^{\frac{p+2}{4}}\xi^{3(1-\frac{p}{2})}\,\epsilon_{e,f}^{p-1} \times \epsilon_{B,f}^{\frac{p-2}{4}}\,E_{54.7}^{\frac{p+2}{4}}\,D_{28}^{-2}\left(\frac{E_\gamma}{100\,{\rm MeV}}\right)^{-\frac{p}{2}}, \quad (10)$$

and $F_{\nu,\rm fl}$ is given in Fraija (2015). The terms $k_f = (1 + Y_f)$ and ξ are parameters defined in Chevalier & Li (2000) and Fraija et al. (2016a) and E is the equivalent kinetic energy. The LC in the slow-cooling regime is

$$[F_{\nu,\rm f}]^{\rm syn} = \begin{cases} F_{\nu,\rm sl}\,t_1^{-\frac{3p-1}{4}}, & E_{\rm m,f}^{\rm syn} < E_\gamma < E_{\rm c,f}^{\rm syn}, \\ F_{\nu,\rm sh}\,t_1^{-\frac{3p-2}{4}}, & E_{\rm c,f}^{\rm syn} < E_\gamma < E_{\rm max,f}^{\rm syn}, \end{cases} \quad (11)$$

with $F_{\nu,\rm sh}$ and $F_{\nu,\rm sl}$ given by

$$F_{\nu,\rm sh} = 1.9 \times 10^5\,{\rm mJy}\,k_f^{-1}(1+z)^{\frac{p+2}{4}}\,\xi^{3(1-\frac{p}{2})}\epsilon_{e,f}^{p-1}\,\epsilon_{B,f}^{\frac{p-2}{4}} \times E_{54.7}^{\frac{p+2}{4}}\,D_{28}^{-2}\left(\frac{E_\gamma}{10\,{\rm keV}}\right)^{-\frac{p}{2}}, \quad (12)$$

and

$$F_{\nu,\rm sl} \simeq 7.4 \times 10^7\,{\rm mJy}(1+z)^{\frac{p+5}{4}}\xi^{\frac{(1-3p)}{2}}\epsilon_{e,f}^{p-1}\,\epsilon_{B,f}^{\frac{p+1}{4}}\,A_\star \times E_{54.7}^{\frac{p+1}{4}}\,D_{28}^{-2}\left(\frac{E_\gamma}{2\,{\rm eV}}\right)^{\frac{1-p}{2}}, \quad (13)$$

respectively. The transition time between fast- and slow-cooling regime occurs at $t_0^{\rm syn} = 2.3 \times 10^7{\rm s}\left(\frac{1+z}{1.34}\right)\xi_{-0.3}^{-4}\epsilon_{e,f}\,\epsilon_{B,f}\,A_\star$.

3.3.2. Light Curves from Reverse Shock Emission

Synchrotron LCs are derived in Kobayashi (2000). The synchrotron fast-cooling regimen is (Kobayashi & Zhang 2003)

$$[F_{\nu,\rm r}]^{\rm syn} \propto \begin{cases} t^{\frac{1}{2}}, & t < t_d, \\ t^{-3}, & t > t_d, \end{cases} \quad (14)$$

where t_d is the crossing time. The synchrotron flux at the deceleration time is give by

$$F_{\gamma,\rm peak,r}^{\rm syn} \simeq 2.3 \times 10^4\,{\rm mJy}\,(1+z)^{5/4}\,k_r^{-1}\,\xi^{\frac{1}{2}}\epsilon_{B,r}^{-\frac{1}{4}}\,\Gamma_{2,r}^{-1}\,A_\star^{-\frac{1}{2}} \times D_{28}^{-2}\,E_{54.7}^{\frac{5}{4}}\,t_{d,1}^{-\frac{3}{4}}\left(\frac{E_\gamma}{2\,{\rm eV}}\right)^{-1/2}. \quad (15)$$

The LC of Compton scattering emission is analytically derived in Fraija (2015). It is written as

$$[F_{\nu,\rm r}]^{\rm ssc} \propto \begin{cases} t^{\frac{1}{2}}, & t < t_d, \\ t^{-\frac{p-1}{2}}, & t > t_d. \end{cases} \quad (16)$$

It is worth noting that the decay index of the emission for $t > t_d$ might be higher than $\frac{p-1}{2}$ due to the angular time delay effect (Kobayashi & Zhang 2003). The SSC flux peaks at

$$F_{\gamma,\rm peak,r}^{\rm ssc} \simeq 2.1 \times 10^{-2}\,{\rm mJy}(1+z)^{-\frac{1}{2}}\xi^9\,Y_r\,k_r^{-5}\,\epsilon_{e,r}\,\epsilon_{B,r}^{-\frac{7}{2}}\,\Gamma_{2,r}^{-6} \times A_\star^{-6}\,D_{28}^{-2}\,E_{54.7}\,t_{d,1}^{-\frac{1}{2}}\left(\frac{E_\gamma}{100\,{\rm MeV}}\right)^{-\frac{1}{2}}. \quad (17)$$

Table 2
Parameters Found after Fitting the Multiwavelength Observations with an Internal Shock Model

	GRB 080319B		GRB 130427A	
Synchrotron Radiation				
$E_{\gamma,\rm p}^{\rm syn}$ (eV)	0.7	1.4	0.7	1.4
γ_e	$10^{2.98}$	$10^{2.83}$	$10^{3.03}$	$10^{2.88}$
Y_1	101.2	100.7	297.9	299.7
B' (G)	0.5	2.1	0.3	1.2
$\tau(\times 10^{-4})$	1.1	2.2	2.7	5.1
$R(\times 10^{15}$ cm)	11.8	2.9	2.8	7.4
$N_e(\times 10^{53})$	2.9	0.3	39.5	5.3
SSC1				
α	0.833	0.833	0.789	0.789
β	3.499	3.499	3.06	3.06
$E_{\gamma,\rm p}^{\rm ssc1}$ (keV)	651	651	830	830
SSC2				
Y_2 (Theor.)	6.1	12.3	25.3	35.6
Y_2 (Observ.)	$\lesssim$2.2	$\lesssim$4.1	$\lesssim$3.9	$\lesssim$8.8
$E_{\gamma,\rm p}^{\rm ssc2}$ (GeV)	605.4	302.7	984.1	492.1

4. Discussion

We have introduced two scenarios for the origin of the early optical flashes present in GRB 080319B and GRB 130427A. In the IS scenario, the optical flash and the MeV γ-ray emission are correlated through the SSC model whereas in the early-afterglow ES scenario the optical flash is studied together with the multiwavelength afterglow observations.

4.1. Internal Shocks

In this scenario, we have assumed that the bright optical flash can be interpreted as synchrotron radiation and the MeV γ-ray component as the IC scattering of the synchrotron photons by the same population of electrons. We have required the Band function (Band et al. 1993) to interpret the optical flash and to fit the γ-ray component.

Requiring the parameter values of the Band function (α, β, and $E_{\gamma,\rm p}^{\rm ssc1}$) for GRB 0800319B (Racusin et al. 2008b) and GRB 130427A (von Kienlin 2013) that describe the MeV γ-ray components, we compute the values of γ_e that describe the optical data for the synchrotron peak in the range $0.7 < E_{\gamma,\rm p}^{\rm syn} < 1.4$ eV, as shown in Table 2. Additionally, we obtain the values of the the optical thickness, the strength of comoving magnetic field, emitting radius, and the the number of radiating electrons. Because the MeV γ-ray component has a large amount of photons, the radiation process given by the second-order IC scattering must be considered (Kumar & Panaitescu 2008). From the values obtained (see Table 2) after describing the optical flashes and MeV γ-ray components with synchrotron and IC scattering emissions, respectively, we

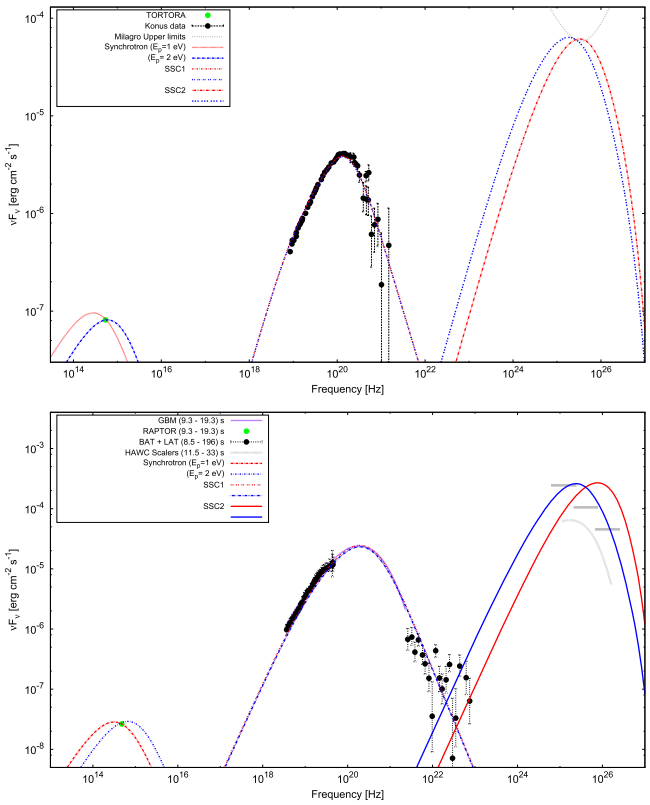

Figure 3. Fits of the SED of GRB 080319B (above) and GRB 130427A (below) observations with SSC model of first- and second-order. Synchrotron emission has been used to describe the optical data and the IC scattering has been used to fit MeV γ-ray data. We require the upper limits placed by the Milagro and HAWC experiments, respectively, to constrain the IC scattering of second order. (For details, see Abdo et al. 2012; Abeysekara et al. 2015a).

compute that the second-order IC scattering peaks in the energy range where Milagro and HAWC observatories are sensitive. Although these TeV experiments did not collect statistically significant excess of counts, upper limits were placed on the GeV–TeV energies. Considering these upper limits and Equations (1) and (8), we have obtained the Compton parameters for the first and second IC scattering. Figure 1 shows the fit of the SED of GRB 080319B (above) and GRB 130427A (below) observations with SSC model of first- and second-order. For the GeV γ-ray fluxes, we have used the effect of the extragalactic background light absorption modeled in Franceschini et al. (2008). As shown in Figure 3, the upper limits set by Milagro and HAWC experiments are useful to constrain the values of the Compton parameters of the second scattering.

Table 2 shows the values of Y_2 obtained from the theoretical model proposed in Kumar & Panaitescu (2008) and from the upper limits set by Milagro and HAWC experiments. The theoretical value of Y_2 was calculated with $\Gamma = 500$ which was estimated from the variability timescale and the inferred burst radius. Comparing both the theoretical and observational values, one can see that the values of Y_2 obtained with the theoretical model are forbidden, thus indicating that the SSC scenario is disfavored to explain the correlation of optical and the MeV γ-ray emission. This result is consistent with the fact that in the SSC framework, IC scattering must have less fluctuations than the synchrotron photon field; however, the MeV gamma-ray LC shows a higher variability than the optical counterpart. The result of a much lower Compton parameter for the second scattering than the first one (see Table 2) is due to the fact that the KN suppression does not affect the first scattering but does affect the second. From Equations (7) and (8), and using the upper limits derived by Milagro and HAWC observatories, we found that the values allowed of the bulk Lorentz factor for $E^{\rm syn}_{\gamma,{\rm p}} = 0.7\ (1.4)$ eV are $\Gamma \lesssim 180\ (167)$ for GRB 080319B, and $\Gamma \lesssim 77\ (124)$ for GRB 130427A.

On the other hand, using the upper limits on the prompt optical emission, Piran et al. (2009) showed that, under the general conservative assumption, the inverse Compton scattering mechanism suffers from an "energy crisis," which is the overproduction of a VHE component that would carry much more energy than the observed MeV prompt. Authors explored the parameter space to see whether there exists a regime for less energy in the second-order IC component than in the MeV γ-ray prompt. They found that the parameter space for Γ and γ_e is limited to a very small region. In our work, upper limits are set at the TeV–GeV range instead of optical band previously developed in Piran et al. (2009). Therefore, using the fit of the optical and MeV γ-ray data, we found that the flux ratio is $\frac{F^{\rm ssc1}_\nu}{F^{\rm syn}_\nu} \approx 10^{-3}$, which is much smaller than that analysis performed in Piran et al. (2009) $\left(\frac{F^{\rm ssc1}_\nu}{F^{\rm syn}_\nu} = 10^{-2}\right)$ and Yost et al. (2007) $\left(\frac{F^{\rm ssc1}_\nu}{F^{\rm syn}_\nu} \gtrsim 0.1\right)$. Considering the condition $E^{\rm ssc2}_{\gamma,{\rm p}}\, F^{\rm ssc2}_\nu \lesssim E^{\rm ssc1}_{\gamma,{\rm p}}\, F^{\rm ssc1}_\nu$ ($Y_2 \lesssim 1$), we found that the values allowed of the bulk Lorentz factors for $E^{\rm syn}_{\gamma,{\rm p}} = 0.7\ (1.4)$ eV lie at $\Gamma \lesssim 8.2\ (4.1)$ for GRB 080319B and $\Gamma \lesssim 20\ (14)$ for GRB 130427A.

We show that the Lorentz factors calculated using the upper limits set by Milagro and HAWC observatories are much less than that obtained by theoretical considerations (Kumar & Panaitescu 2008). This inconsistency illustrates that optical flashes are not correlated with the γ-ray components, and hence produced likely by different electron populations.

4.2. Early-afterglow External Shocks

In this scenario, we use the early-afterglow ES model presented in Fraija et al. (2016a) in order to fit the early optical flashes together with the multiwavelength data observed in GRB 0803189B and GRB 130427A. From the deceleration timescales $t_{\rm dec} = 10$ s (GRB 130427A) and 50 s (GRB 080319B), the values of bulk Lorentz factors are $\Gamma = 520$ and $\Gamma = 550$ for stellar densities $A = 10^{10}\,{\rm g\,cm^{-1}}$ and $5 \times 10^{10}\,{\rm g\,cm^{-1}}$, respectively.

In order to obtain the values of microphysical parameters, the optical flashes and the multiwavelength data are fitted using the χ^2 test (Brun & Rademakers 1997). Figure 4 (upper panel) displays the microphysical parameter space ($\epsilon_{B,f}$, $\epsilon_{e,f}$) that reproduces the long-lived emissions for $p = 2.2$. The value of the power index of the electron distribution was obtained through the closure relation of synchrotron flux ($F_\nu \propto t^{-\alpha}\nu^{-\beta}$) with the observed slopes of temporal decays of X-ray ($\alpha_X = 1.31 \pm 0.03$; Kumar & Panaitescu 2008) and optical ($\alpha_{3,{\rm Opt}} = 1.25 \pm 0.02$; Racusin et al. 2008b) fluxes for GRB 080319B and GeV γ-ray ($\alpha_{\rm GeV} = -1.17 \pm 0.06$; Ackermann et al. 2014), X-ray ($\alpha_{\rm X} = -1.29^{+0.02}_{-0.01}$; Maselli et al. 2014) and optical ($\alpha_{\rm opt} = -1.67 \pm 0.07$; Vestrand et al. 2014) fluxes for GRB 130427A. The optical flux of GRB 080319B afterglow at 10^3 s was extrapolated to earlier times considering that it was eclipsed for the optical flux from RS (Kumar &

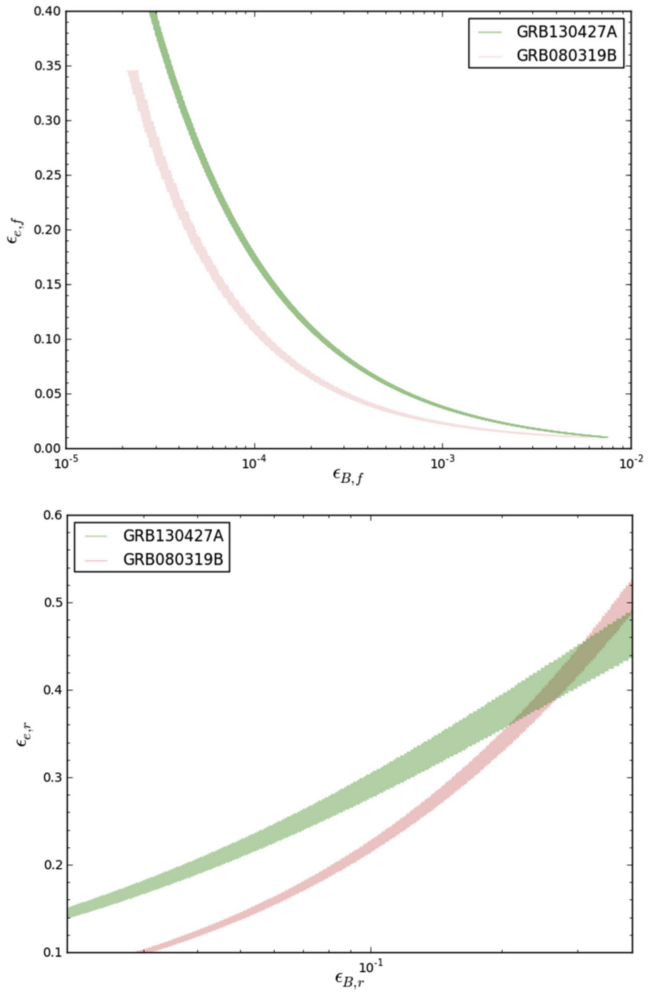

Figure 4. Microphysical parameter space that describes the temporally extended emissions (panel above) and the brightest optical flashes (panel above) present in GRB 080319B and GRB 130427A.

Panaitescu 2008). The lower panel exhibits the microphysical parameter space ($\epsilon_{B,r}$, $\epsilon_{e,\ r}$), which describes the bright optical flashes. Although we adjust the bright LAT peak in GRB 130427A (see Fraija et al. 2016a), the microphysical parameter region found for describing this LAT peak is not included. It was done to display the similarities between the parameter spaces for both bursts. The extended fluxes have been fitted using the synchrotron radiation from FS and the bright peaks with synchrotron radiation from RS. The optical fluxes with power index $\alpha_{2,\rm Opt} = 2.24 \pm 0.03$ (Kumar & Panaitescu 2008) can be explained with the LC of synchrotron emission from RS.

In Table 3, we summarize the microphysical parameters, the stellar wind densities and the bulk Lorentz factors found after fitting the multiwavelength data from GRB 130427A and GRB 080319B. Computing the magnetisation parameter, one can see that it lies in the range ($0.1 \leqslant \sigma \leqslant 1$), which is consistent with the description of the bright peak from RS and the duration of shock crossing time shorter than T_{90} (Zhang et al. 2003; Fan et al. 2004; Fraija et al. 2016b, 2017a). Otherwise, when the GRB outflow crossed the RS, it would have been suppressed (Fan et al. 2004; Zhang & Kobayashi 2005).

Using the values of parameters reported in Table 3, the observable quantities have been computed, as shown in Table 4.

Table 3
Parameters Found after Fitting the Multiwavelength Data with the Early-afterglow ES Model

	GRB 080319B	GRB 130427A
Forward Shock		
$\epsilon_{B,f}$	5×10^{-5}	3×10^{-5}
ϵ_e	0.3	0.32
A (10^{10} g cm^{-1})	1	5
Γ	520	550
Reverse Shock		
$\epsilon_{B,r}$	0.15	0.13
ϵ_e	0.3	0.32
$A(10^{10}$ g cm$^{-1})$	1	5
Γ	520	550

Table 4
Observable Quantities Obtained with the Parameters Reported in Table 3 and the ES Model

	GRB 080319B	GRB 130427A
Forward Shock		
$t_{\rm dec}$ (s)	22.5	9.9
B'_f (G)	0.5	18.9
Synchrotron Emission		
$E^{\rm syn}_{\gamma,{\rm a,f}}$ (eV)	2.7×10^{-4}	3.3×10^{-2}
$E^{\rm syn}_{\gamma,{\rm m,f}}$ (keV)	1.3	23.1
$E^{\rm syn}_{\gamma,{\rm c,f}}$ (eV)	245.6	1.3
$E^{\rm syn}_{\gamma,{\rm max,f}}$ (GeV)	6.5	107.7
SSC Emission		
$E^{\rm ssc}_{\gamma,{\rm m,f}}$ (TeV)	0.4	22.1
$E^{\rm ssc}_{\gamma,{\rm c,f}}$ (TeV)	0.4	1.4×10^{-7}
$E^{\rm KN}_{\gamma,{\rm f}}$ (GeV)	5.4×10^{3}	102.3
Reverse Shock		
Γ_c	321.8	236.7
B'_r (G)	21.2	1.7×10^{3}
Synchrotron Emission		
$E^{\rm syn}_{\gamma,{\rm a,r}}$ (eV)	1.41×10^{-9}	0.5×10^{-7}
$E^{\rm syn}_{\gamma,{\rm m,r}}$ (eV)	1.2	14.3
$E^{\rm syn}_{\gamma,{\rm c,r}}$ (eV)	0.3	2.5×10^{-5}
SSC Emission		
$E^{\rm ssc}_{\gamma,{\rm m,r}}$ (MeV)	1.8	61.2
$E^{\rm ssc}_{\gamma,{\rm c,r}}$ (eV)	11.5×10^{3}	1.4×10^{-5}
$E^{\rm KN}_{\gamma,{\rm r}}$ (GeV)	38.3×10^{3}	166.2

In this table, some features can be observed: (i) Comparing the values of synchrotron spectral breaks from RS, one can see that the synchrotron spectrum lies in the fast-cooling regime for both GRB 080319B ($E^{\rm syn}_{\gamma,{\rm c,r}} \lesssim E^{\rm syn}_{\gamma,{\rm m,r}}$) and GRB 130427A ($E^{\rm syn}_{\gamma,{\rm c,r}} \ll E^{\rm syn}_{\gamma,{\rm m,r}}$). Once the period where the optical and the γ-ray components exhibited close correlations have finished ($t \gtrsim$ 60 s), the synchrotron spectrum of GRB 080319B changes from

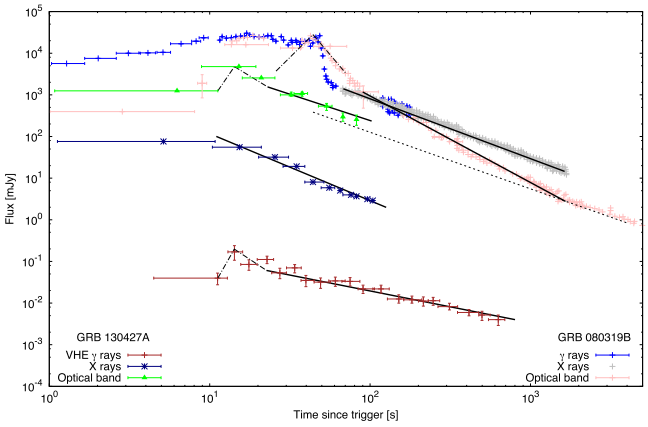

Figure 5. γ-ray, X-ray, and optical LCs of GRB 080319B and GRB 130427A. The combine X-ray and *Swift*-BAT data are extrapolated down into the XRT energy range (0.3–10 keV).

the fast to slow-cooling regime ($E^{\rm syn}_{\gamma,{\rm m,r}} \lesssim E^{\rm syn}_{\gamma,{\rm c,r}}$), producing a temporal power index of $\frac{3(5p+1)}{16} = 22.5$ and the synchrotron spectrum of GRB 080319B keeps in the fast-cooling regime. It explains the different behavior of the optical flux after the optical flashes. (ii) The values of the characteristic SSC energies ($E^{\rm ssc}_{\gamma,{\rm m,r}}$) illustrate that whereas a peak at $\sim$100 MeV can be detected in GRB 130427A, just a peak at much lower energies $\sim$2 MeV can be observed in GRB 080319B. (iii) From the strength of magnetic fields derived in the forward- and reverse shock regions can be seen that the ejecta of both bursts are magnetized.

Figure 5 shows the contributions of synchrotron radiation from FS and RS to the multiwavelength afterglow observed in GRB 080319B and GRB 130427A.

5. Conclusions

Both GRB 080319B and GRB 130427A are among the most powerful bursts detected in optical and γ-ray energy bands. The exceedingly bright optical emission peaking with the γ-ray components at the early phase of these bursts pose challenges in the theoretical models for IS and/or RS.

In the IS framework, the most natural explanation for the spectral energy distribution of GRB 080319B and GRB 130427A is to interpret the optical flashes by synchrotron emission and the MeV γ-ray photons by IC scattering. Due to the huge amount of MeV γ-ray photons, the SSC model predicts the existence of a strong peak at hundreds of GeV. Although no significant excess of counts coming from these bursts were observed by Milagro and HAWC observatories, upper limits were used to constrain this model. We show that the HAWC and Milagro upper limits are restrictive when the second -order IC scattering model is considered. From the value of the second-order Compton parameter found using our model and the parameter space allowed for the bulk Lorentz factors, we conclude that the optical and the MeV γ-ray components are produced by different electron populations, thus disfavoring the IS scenario. Our analysis was focused on the case that the optical flashes were created within the emitting region that includes the IC scattering ultra-relativistic electrons. This analysis was limited to the important implicit assumption that the moving region is homogenous. It is worth noting that very strong inhomogeneities might change this scenery.

In the early-afterglow picture, we have used the leptonic model introduced in Fraija et al. (2016a) in order to describe the bright optical flashes. These have been interpreted as the synchrotron FS emission in the thick-shell case. Considering that the ejecta propagating into the stellar wind is decelerated early, at $\sim$50 s and $\sim$10 s for GRB 080319B and GRB 130427A, respectively, we found that the value of the bulk Lorentz factor, as required for most powerful lGRBs, lies in the range ($\Gamma \sim$ 500–550; Veres & Mészáros 2012; Ackermann et al. 2013, 2014; Fraija et al. 2017b, 2017c). The set of parameters has been limited considering the multiwavelength data. To find the values of microphysical parameters ($\epsilon_{B,f/r}$, ϵ_e), we have assumed that these are constant in the description of the multiwavelength afterglow data. The long-lived (LAT, X-ray, and optical) emissions was modeled with synchrotron FS radiation and the bright optical flashes with synchrotron RS emission from RS.

Since GRB 080319B and GRB 130427A are the most energetic bursts observed with $z \leqslant 1.0$, a large amount of target optical photons is created so that hadrons in the outflow can interact efficiently. Therefore, these bursts represent potential sources to produce neutrinos with energies between the TeV and PeV range. Searches with IceCube telescope for TeV—PeV muon neutrinos were performed around GRB 0800319B (Abbasi et al. 2009) and GRB 130427A (Blaufuss 2013) without collecting excess above background. Some authors have investigated the possible correlation between the lack of neutrinos and the strengths of magnetic fields (Zhang & Kumar 2013; Fraija 2014). If this is true, the null result reported by this neutrino observatory might be interpreted in terms of the levels of magnetizations found in this paper for both bursts.

Some authors have claimed that the γ-ray emission detected by LAT during the prompt phase has an internal origin similar to the optical counterpart (He et al. 2011; Liu & Wang 2011; Maxham et al. 2011; Zhang et al. 2011). However, by completing the analysis with the upper limits reported by Milagro and HAWC observatories, we have shown that the optical flashes and the γ-ray components are not produced by the same electron population. Therefore, there is overwhelming evidence that the bright optical flashes come from the RS, as has been explained in this work. It is important to highlight that, although no significant excess of counts have been detected from both bursts by these TeV γ-ray observatories, nowadays, bursts with identical features can be detected by this HAWC experiment (Abeysekara et al. 2012, 2015b; Wood & for the HAWC Collaboration 2015; Lennarz & Taboada 2015). It is worth noting that although GRB 990123 exhibited a bright optical flash (Akerlof et al. 1999), no correlation with gamma-rays was reported (Kobayashi & Zhang 2003; Mészáros & Rees 1999; Sari & Piran 1999) and no upper limits were placed by TeV observatories. Therefore, similar bursts could bring to light information on external medium density, bulk Lorentz factors and energy fractions converted to accelerate electron and/or amplify magnetic fields, thus potentially further constraining possible models.

We thank Dirk Lennarz, Ignacio Taboada, Fabio de Colle, and Anatoly Spitovsky for useful discussions. This work was supported by PAPIIT-UNAM IA102917 and Fermi grant NNM11AA01A (PV).

ORCID iDs

N. Fraija https://orcid.org/0000-0002-0173-6453
P. Veres https://orcid.org/0000-0002-2149-9846

References

Abbasi, R., Abdou, Y., Abu-Zayyad, T., et al. 2009, ApJ, 701, 1721
Abdo, A. A., Abeysekara, A. U., Allen, B. T., et al. 2012, ApJL, 753, L31
Abeysekara, A. U., Aguilar, J. A., Aguilar, S., et al. 2012, APh, 35, 641
Abeysekara, A. U., Alfaro, R., Alvarez, C., et al. 2015a, ApJ, 800, 78
Abeysekara, A. U., Alfaro, R., Alvarez, C., et al. 2015b, ApJ, 800, 78
Ackermann, M., Ajello, M., Asano, K., et al. 2013, ApJ, 763, 71
Ackermann, M., Ajello, M., Asano, K., et al. 2014, Sci, 343, 42
Akerlof, C., Balsano, R., Barthelmy, S., et al. 1999, Natur, 398, 400
Ando, S., Nakar, E., & Sari, R. 2008, ApJ, 689, 1150
Asano, K., & Inoue, S. 2007, ApJ, 671, 645
Band, D., Matteson, J., Ford, L., et al. 1993, ApJ, 413, 281
Beloborodov, A. M. 2002, ApJ, 565, 808
Blaufuss, E. 2013, GCN, 14520, 1
Bloom, J. S., Perley, D. A., Li, W., et al. 2009, ApJ, 691, 723
Brun, R., & Rademakers, F. 1997, NIMPA, 389, 81
Chevalier, R. A., & Li, Z.-Y. 2000, ApJ, 536, 195
Cohen, E., Katz, J. I., Piran, T., et al. 1997, ApJ, 488, 330
Cwiok, M., Dominik, W., Kasprowicz, G., et al. 2008, GCN, 7439, 1
Ćwiok, M., Dominik, W., Małek, K., et al. 2007, Ap&SS, 309, 531
Eichler, D., Livio, M., Piran, T., & Schramm, D. N. 1989, Natur, 340, 126
Fan, Y. Z., Wei, D. M., & Wang, C. F. 2004, A&A, 424, 477
Flores, H., Covino, S., Xu, D., et al. 2013, GCN, 14491, 1
Fraija, N. 2014, ApJ, 787, 140
Fraija, N. 2015, ApJ, 804, 105
Fraija, N., De Colle, F., Veres, P., et al. 2017a, arXiv:1710.08514
Fraija, N., Lee, W., & Veres, P. 2016a, ApJ, 818, 190
Fraija, N., Lee, W. H., Araya, M., et al. 2017b, ApJ, 848, 94
Fraija, N., Lee, W. H., Veres, P., & Barniol Duran, R. 2016b, ApJ, 831, 22
Fraija, N., Veres, P., Zhang, B. B., et al. 2017c, ApJ, 848, 15
Franceschini, A., Rodighiero, G., & Vaccari, M. 2008, A&A, 487, 837
Gao, H., Lei, W.-H., Zou, Y.-C., Wu, X.-F., & Zhang, B. 2013, NewAR, 57, 141
Genet, F., Daigne, F., & Mochkovitch, R. 2007, MNRAS, 381, 732
Ghisellini, G., Lazzati, D., Celotti, A., & Rees, M. J. 2000, MNRAS, 316, L45
Golenetskii, S., Aptekar, R., Frederiks, D., et al. 2013, GCN, 14487, 1
Golenetskii, S., Aptekar, R., Mazets, E., et al. 2008, GCN, 7482, 1
Guetta, D., & Granot, J. 2003, ApJ, 585, 885
Gupta, N., & Zhang, B. 2007, MNRAS, 380, 78
He, H.-N., Wu, X.-F., Toma, K., Wang, X.-Y., & Mészáros, P. 2011, ApJ, 733, 22
Hjorth, J., & Bloom, J. S. 2012, in Gamma-Ray Bursts, ed. C. Kouveliotou, R. A. M. J. Wijers, & S. Woosley (Cambridge: Cambridge Univ. Press), 169
Hjorth, J., Sollerman, J., Møller, P., et al. 2003, Natur, 423, 847
Kawamuro, T., Shidatsu, M., Nakahira, S., et al. 2013, GCN, 14462, 1
Kobayashi, S. 2000, ApJ, 545, 807
Kobayashi, S., & Zhang, B. 2003, ApJ, 597, 455
Kouveliotou, C., Granot, J., Racusin, J. L., et al. 2013, ApJL, 779, L1
Kumar, P., & McMahon, E. 2008, MNRAS, 384, 33
Kumar, P., & Panaitescu, A. 2008, MNRAS, 391, L19
Kumar, P., & Piran, T. 2000, ApJ, 532, 286
Kumar, P., & Zhang, B. 2015, PhR, 561, 1
Lee, W. H., Ramirez-Ruiz, E., & Page, D. 2004, ApJL, 608, L5
Lee, W. H., Ramirez-Ruiz, E., & Page, D. 2005, ApJ, 632, 421
Lennarz, D., & Taboada, I. 2013, GCN, 14549, 1
Lennarz, D., & Taboada, I. 2015, arXiv:1508.07325
Levan, A. J., Fruchter, A. S., Graham, J., et al. 2013, GCN, 14686, 1
Liu, R.-Y., & Wang, X.-Y. 2011, ApJ, 730, 1
Maselli, A., Melandri, A., Nava, L., et al. 2014, Sci, 343, 48
Maxham, A., Zhang, B.-B., & Zhang, B. 2011, MNRAS, 415, 77
Mészáros, P., Ramirez-Ruiz, E., & Rees, M. J. 2001, ApJ, 554, 660
Meszaros, P., & Rees, M. J. 1994, MNRAS, 269, L41
Mészáros, P., & Rees, M. J. 1997, ApJ, 476, 232
Mészáros, P., & Rees, M. J. 1999, MNRAS, 306, L39
Narayan, R., Paczynski, B., & Piran, T. 1992, ApJL, 395, L83
Pagani, C., Racusin, J. L., Holland, S. T., & Barhtelmy, S. D. 2008, GCNR, 121, 1
Panaitescu, A., & Kumar, P. 2002, ApJ, 571, 779
Panaitescu, A., & Mészáros, P. 2000, ApJL, 544, L17
Pe'er, A., & Waxman, E. 2004, ApJ, 613, 448
Piran, T., Sari, R., & Zou, Y.-C. 2009, MNRAS, 393, 1107
Pozanenko, A., Minaev, P., & Volnova, A. 2013, GCN, 14484, 1
Preece, R. D., Briggs, M. S., Giblin, T. W., et al. 2002, ApJ, 581, 1248
Preece, R. D., Briggs, M. S., Mallozzi, R. S., et al. 1998, ApJL, 506, L23
Racusin, J. L., Gehrels, N., Holland, S. T., et al. 2008a, GCN, 7427, 1
Racusin, J. L., Karpov, S. V., Sokolowski, M., et al. 2008b, Natur, 455, 183
Rees, M. J., & Meszaros, P. 1992, MNRAS, 258, 41P
Rees, M. J., & Meszaros, P. 1994, ApJL, 430, L93
Sari, R., & Piran, T. 1999, ApJL, 517, L109
Smith, D. M., Csillaghy, A., Hurley, K., et al. 2013, GCN, 14590, 1
Taylor, G. B., Frail, D. A., Berger, E., & Kulkarni, S. R. 2004, ApJL, 609, L1
Uhm, Z. L., & Beloborodov, A. M. 2007, ApJL, 665, L93
Veres, P., & Mészáros, P. 2012, ApJ, 755, 12
Verrecchia, F., Pittori, C., Giuliani, A., et al. 2013, GCN, 14515, 1
Vestrand, W. T., Wren, J. A., Panaitescu, A., et al. 2014, Sci, 343, 38
von Kienlin, A. 2013, GCN, 14473, 1
Wood, J. & for the HAWC Collaboration 2015, arXiv:1508.04120
Woosley, S. E., & Bloom, J. S. 2006, ARA&A, 44, 507
Wren, J., Vestrand, W. T., Wozniak, P., & Davis, H. 2010, Proc. SPIE, 7737, 773723
Xu, D., de Ugarte Postigo, A., Leloudas, G., et al. 2013, ApJ, 776, 98
Yost, S. A., Aharonian, F., Akerlof, C. W., et al. 2007, ApJ, 669, 1107
Zerbi, R. M., Chincarini, G., Ghisellini, G., et al. 2001, AN, 322, 275
Zhang, B., & Kobayashi, S. 2005, ApJ, 628, 315
Zhang, B., Kobayashi, S., & Mészáros, P. 2003, ApJ, 595, 950
Zhang, B., & Kumar, P. 2013, PhRvL, 110, 121101
Zhang, B.-B., Uhm, Z. L., Connaughton, V., Briggs, M. S., & Zhang, B. 2016, ApJ, 816, 72
Zhang, B.-B., Zhang, B., Liang, E.-W., et al. 2011, ApJ, 730, 141
Zou, Y.-C., Piran, T., & Sari, R. 2009, ApJL, 692, L92